Supporting Information for

Incorporation of Cr^{III} into a Keggin polyoxometalate as a chemical strategy to stabilize a labile $\{Cr^{III}O_4\}$ tetrahedral conformation and promote unattended single-ion magnet properties

Nadiia I. Gumerova,[†] Alexander Roller,[‡] Gerald Giester,[§] J. Krzystek,[¶] Joan Cano[‖] and Annette Rompel*[†]

[†] Universität Wien, Fakultät für Chemie, Institut für Biophysikalische Chemie, 1090 Vienna, Austria, www.bpc.univie.ac.at
[‡] Universität Wien, Fakultät für Chemie, Zentrum für Röntgenstrukturanalyse, 1090 Vienna, Austria
[§] Universität Wien, Fakultät für Geowissenschaften, Geographie und Astronomie, Institut für Mineralogie und Kristallographie, 1090 Vienna, Austria
[¶] National High Magnetic Field Laboratory, Florida State University, Tallahassee, Florida 32310, United States
[‖] Department of Química Inorgànica/Instituto de Ciencia Molecular (ICMol), Facultat de Quimica de la Universitat de València, C/Catedrático Jose Beltrán 2, 46980 Paterna, València, Spain
*Correspondence to annette.rompel@univie.ac.at

Table of Contents

Materials and Methods

The chemicals were of reagent grade and used as purchased without further purification. Ammonium metatungstate $(NH_4)_6[H_2W_{12}O_{40}]\cdot 3H_2O$ (WO_3 content found (calculated): 92.5 % (92.4 %)) was provided by Global Tungsten & Powders Corp.

Physical methods

Infrared spectrum (4000−400 cm^{-1}) of the sample was recorded on a Bruker Vertex 70 IR Spectrometer equipped with a single-reflection diamond-ATR unit. *Elemental analyses* were performed in aqueous solutions containing 2% HNO_3 using inductively coupled plasma mass spectrometry (PerkinElmer Elan 6000 ICP MS) for Cr and W, and atomic absorption spectroscopy (PerkinElmer 1100 Flame AAS) for Na. Standards were prepared from single-element standard solutions of concentration 1000 $mg\cdot l^{-1}$ (Merck, Ultra Scientific and Analytika Prague). Water content was determined *by thermal gravimetric analysis (TGA)* with a Mettler SDTA851e Thermogravimetric Analyzer under air flow with a heating rate of 5 K min^{-1} in the region 298−1023 K. *Mass spectrometry* was performed with an ESI−Qq−oaRTOF supplied by Bruker Daltonics Ltd. Bruker Daltonics Data Analysis software was used to analyze the results. The measurement was carried out in a 1:1 mixture of H_2O/CH_3CN/MeOH, collected in negative ion mode and with the spectrometer calibrated with the standard tune−mix to give an accuracy of ca. 5 ppm in the region of m/z 300−3000. *Cyclic voltammetry* measurements were carried out using a HEKA PG 390 potentiostat at room temperature. A conventional three electrode glass cell of 3 ml capacity was used. A 2 mm diameter glassy carbon disk electrode was used as working electrode (GCE). A platinum wire served as the counter electrode and a normal hydrogen electrode (NHE) as the reference electrode. All solutions were deoxygenated using argon gas for 10-15 min prior to electrochemical experiments. *X-ray powder diffraction* was performed on a Bruker D8 advance diffractometer, Cu Kα radiation, λ = 1.54056 Å, Lynxeye silicon strip detector and SolX energy dispersive detector, variable slit aperture with 12 mm, $8^o \leq 2\theta \leq 50^o$. The *diffuse reflectance spectrum* of a powder sample of **CrW_{12}** was recorded in the range from 190 to 2550 nm and a step of 1 nm using a double-beam V-670 UV-Visible/NIR spectrophotometer equipped with a unique single monochromator, a horizontal sampling integrating sphere PIN-757, PMT and Peltier-cooled PbS detectors for the UV to visible and the NIR regions, respectively.

Synthesis of $Na_{2.4}(C_4H_{12}N)_3[CrW_{12}O_{40}]_{0.6}[H_2W_{12}O_{40}]_{0.4}\cdot 37H_2O$ (CrW_{12}).

A sample of $Na_2WO_4\cdot 2H_2O$ (0.33 g, 1 mmol) was dissolved in water (50 mL) and HCl [1.0 M] (1.2 mL) was added. $Cr(NO_3)_2\cdot 9H_2O$ (0.0417 g, 0.1 mmol) was dissolved in water (2 mL) and added dropwise to the acidified solution of Na_2WO_4. The reaction mixture was heated to reflux followed by addition of *tris*(hydroxymethyl)aminomethane (0.1 g, 0.8 mmol). The final ratio of reagents was 1 Cr : 10 W : 12 H^+ : 5 Tris-NH_2. The excess of chromium salt was used to increase the occupancy of Cr^{III} in the Keggin anion. The final pH was 7.5. After refluxing for 24 hours, TMA−Cl was added (0.55 g, 5 mmol) and the solution was cooled to room temperature. The formation of double salt could be connected to the too high solubility of pure TMA-CrW_{12} salt and necessity of several Na^+ ions for crystallization. Yellow crystals were isolated after 2 weeks. Yield: 83 mg (31 % based on W). Elemental analysis found (calculated) for $Na_{2.4}C_{12}H_{110.8}N_3Cr_{0.6}O_{77}W_{12}$: Na 1.37 (1.43), Cr 1.17 (0.82), W 56.2 (57.7). Elements ratio found (calculated): Na : Cr : W = 2.34 (2.4) : 0.88 (0.6) : 12 (12). IR: 3365 (b), 3024 (m), 1645 (m), 1488 (s), 1419 (m), 1342 (m), 1056 (m), 948 (s), 877 (m), 794 (m), 715 (m), 646 (s), 528 (s), 455 (s) cm^{-1}. *Please note:* The Cr^{III} content might slightly vary in different preparations. Four crystals from different batches were measured and X-ray structure analysis revealed no higher Cr occupancy than 60 % and the same disorder of the central ion. The comparison of theoretical and experiential $\chi_M T$ values points also to partial (36 %) occupancy of the Cr^{III} sites. The possible reaction routes in the Cr^{III}-WO_4^{2-} system between pH 7.5 and 8 applying different Cr and W molar ratios are shown in Scheme S1. The use of NaOH or phosphate buffer to

reach pH 7.5 in the system with the ratio 1.2 Cr : 12 W does not lead to any product isolation and **CrW_{12}** could crystallize only from the Tris buffered solution. From the system with the ratio 1 Cr: 6 W (pH = 7.7), the tris-functionalized Anderson-type POT was isolated under hydrothermal conditions.[1] At pH 8 crystallization of the unfunctionalized Anderson-type anion is formed.[1] Scheme S1 highlights the complex nature of processes in the Cr-W system and the important influence of pH and Cr to W ratio for end product formation.

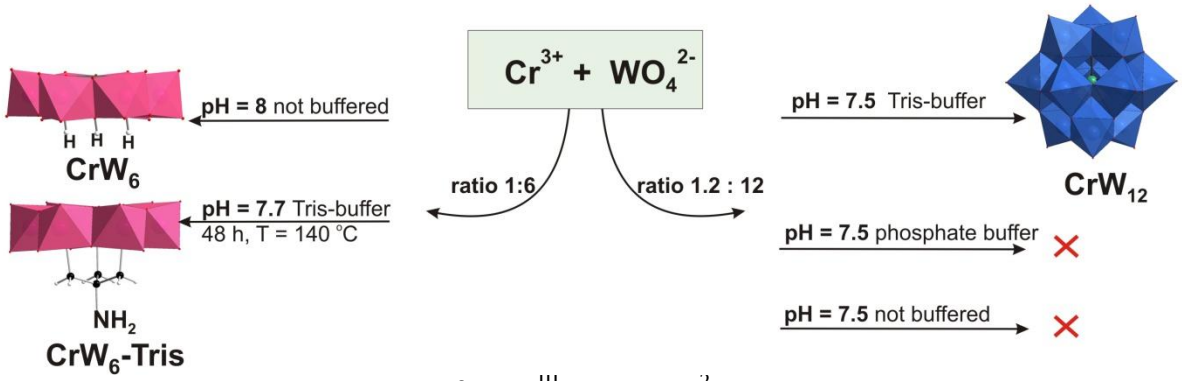

Scheme S1. Possible synthetic routes for Cr^{III} and WO_4^{2-} between pH 7.5 and 8 applying two different molar ratios (1:6 and 1.2:12) in the presence and absence of buffering power. The scheme is based on results obtained in this paper and in [1]. Color code: {WO_6}, blue or pink; Cr, green; O, red.

Computational Details

DFT calculations were carried out through the Gaussian 09 package in order to estimate the relative stability of TD and SQ molecular geometries of the Cr^{III} ion in **CrW_{12}**.[2] These calculations were performed with the PBE pure functional,[3] the quadratic convergence approach, a guess function generated with the fragment tool of the same program, and a stability test of the wavefunction. Triple-ζ (TZV) and double-ζ (SV) all-electron basis set proposed by Ahlrichs *et al.* were used for chromium and oxygen atoms, respectively.[4] LanL2DZ pseudopotentials were considered to describe the tungsten atoms.[5] A polarizable continuum model (PCM) was introduced in the calculations with the parameters corresponding to acetonitrile.[6]

In order to estimate the parameters that determine the axial (*D*) and rhombic (*E*) zfs, calculations in an unusual tetrahedral d^3 complex based on complete active space (CASSCF or CAS) methods were performed on **CrW_{12}** molecule with tetrahedral Cr^{III} ion (occup. 1). Yet this mononuclear species conserves the experimental angular dispositions of the ligands around the metal, and the bond lengths were optimized to correctly calibrate the ligand-field strength of the chloride anions. The optimization geometry was carried out with the Gaussian package using the PBE pure functional and the TZV basis set for all atoms.[3,4] The CASSCF calculations were carried out with the version 4.0 of the ORCA program[7] using the TZVP basis set proposed by Ahlrichs[3] and the auxiliary TZV/C Coulomb fitting basis sets.[8] The contributions to zfs from 10 quartet and 20 doublet excited states generated from an active space with seven electrons in five d orbitals were included using an effective Hamiltonian. The *g*-tensors were calculated for the ground Kramers pair using Multireference Configuration Interaction (MRCI) wavefunctions with a first-order perturbation theory on the SOC matrix.[9] RIJCOSX method was used combining resolution of the identity (RI) and "chain of spheres" COSX approximations for the Coulomb and exchange terms, respectively.[10,11]

Magnetic Measurements

Static direct current (dc) and *ac* measurements were carried out on **CrW_{12}** by powdering and restraining the samples to prevent any displacement due to the magnetic anisotropy. Variable-temperature (2.0−300 K) dc magnetic susceptibility under an applied field of 0.25 ($T < 20$ K) and 5.0 kG ($T \geq 20$ K), and variable-field (0–5.0 T) magnetization in the temperature range from 2 to 10 K were recorded with a Quantum Design SQUID magnetometer. Variable-temperature (2.0–10 K) alternating current (ac) magnetic susceptibility measurements under ±5.0 G oscillating field at frequencies in the range of 0.1−10 kHz were carried out on crystalline samples under different applied static dc fields in the range 0.0−2.5 kG with a Quantum Design Physical Property Measurement System (PPMS). The magnetic susceptibility data were corrected for the diamagnetism of the constituent atoms and the sample holder. HFEPR experiments on powdered samples of **CrW_{12}** were performed using the previously described spectrometer,[12] which was modified with a Virginia Diodes (Charlottesville, VA) source operating at 15.5 ± 3 GHz and generating higher frequencies by a cascade of multipliers. X- and Q-band EPR spectra were recorded in the temperature range 4.0-15 K on a Bruker ER 200 spectrometer equipped with a helium cryostat.

X-ray absorption spectroscopy (XAS) experimental setup and X-ray absorption near edge structure (XANES) analysis

XAS experiments were performed at beamline B18 at Diamond Light Source, UK. The ring energy was 3.0 GeV and the ring current 300 mA. The beamline was equipped with a Si(111) monochromator in continuous scan acquisition mode. Higher-energy harmonics were rejected using two Pt-coated Si mirrors at 9 mrad incident angle. The absolute energy calibration was performed using chromium foil. The edge position was determined over the first maximum in the first derivative and used for the energy calibration. A Canberra 36-elements monolithic germanium detector and Xspress2 readout electronics was used for the measurements in fluorescence mode. Spectra were collected from 5800 to 6800 eV in continuous scan mode with a step size of 0.2 eV. The spectra of the compounds are the average of 20 scans.

Initially careful radiation damage studies were performed by studying spectra collected at different time intervals. The pre-edge background was removed by a linear approximation in the range of −30 eV to −150 eV before the Cr K-edge. Spectra were normalized by fitting a linear spline function to the post-edge region in ATHENA. The edge position was determined as the maximum in the first derivative of the spectrum (inflection point of the steeply rising edge).

X-ray photoelectron spectroscopy (XPS)

The X-ray photoelectron spectra including a survey scan (0–1350 eV) and high-resolution spectra of Cr2p binding energies were recorded on a Thermo Fisher Scientific K-Alpha spectrophotometer (University of Valencia). The spectra were calibrated with the line C1s corresponding to a single C–C bond at 284.84 eV. The analysis of the spectrum (Fig. S13) was achieved by a deconvolution using a mixture of Gaussian and Lorentzian curves in the ratio 0.7:0.3.

X-ray Diffraction on Single Crystals

The X-ray data were measured on a Bruker D8 Venture equipped with a multilayer monochromator, MoKα INCOATEC micro focus sealed tube and Kryoflex cooling device. The structure was solved by direct methods and refined by full-matrix least-squares. Non-hydrogen atoms were refined with anisotropic displacement parameters. All calculations were performed by the Bruker SHELXTL (v. 5.1) package and in OLEX2.

Crystal structure description

The main bond lengths and angles in **CrW_{12}** are consistent with those reported for other $[XW_{12}O_{40}]^{n-}$ anions. The $W–O_{terminal}$, W–O and $W–O_{tet}$ (O_{tet} – atoms belonging to CrO_8) bond

lengths are in the range of 1.672(11)–1.740(20), 1.837(16)–1.941(16) and 2.283(16)–2.416(18) Å, respectively. The Cr–O_{tet} bond lengths are 1.58(2), 1.62(2) and 1.711(17) Å.

Table S1. Details of data collection and refinement.

	$Na_{2.4}(TMA)_3[CrW_{12}O_{40}]_{0.6}[H_2W_{12}O_{40}]_{0.4}\cdot 37H_2O$
Empirical formula	$Cr_{0.60}O_{40}W_{12}$ [+ solvent]
CCDC-number	1913668
M_r	2877.40
Crystal system	monoclinic
Space group	*C* 2/*m*
T, K	100
a, *b*, *c* (Å)	15.0892(6) 21.1101(6) 13.0805(4)
β (°)	98.788(2)°
V (Å^3)	4117.7(2)
Z	2
D_{calc}, g/cm^3	2.321
μ, mm^{-1}	31.112
Abs. correction type	multiscan
Abs. correction Tmin	0.055
Abs. correction Tmax	0.424
F(000)	2445.0
Crystal size, mm	0.20 × 0.09 × 0.05
Theta range for data collection	3.19° – 32.54
Index ranges	$-17 \le h \le 17$ $-24 \le k \le 24$ $-15 \le l \le 15$
Reflections collected	29032
Independent reflections	3148
Rint	0.0365
Data / restraints / parameters	3593/18/141
Goodness-of-fit	1.086
Final *R* indices	R_F = 0.0724, wR_2 = 0.1857 (all data) R_F = 0.0666, wR_2 = 0.18022 (I>2σ(I))
Largest diff. peak and hole, e. Å^{-3}	2.11/-2.94

IR spectrum

The IR spectrum of **CrW_{12}** shows all bands expected for a classical Keggin structure (Fig. S1): the terminal W=O stretching vibration appears as a strong band at 948 cm^{-1}, the bands associated with asymmetric W–O–W vibrations within the {W_3O_{13}} triplets at 794 cm^{-1}, and those from W–O–W vibrations involving oxygen bridges between adjacent {W_3O_{13}} triplets at 877 cm^{-1}. The deformation vibrations of W–O–Cr bridging fragments are observed at 455 cm^{-1}, and its stretching vibrations are covered by much stronger W–O–W bands.

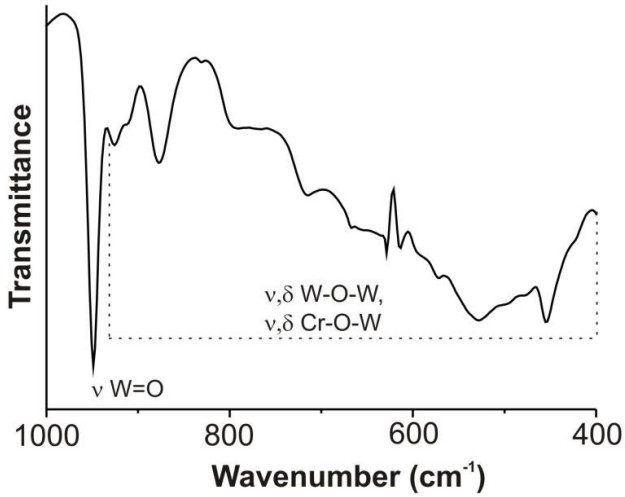

Fig. S1. IR spectrum of **CrW_{12}**.

Electrospray ionization mass spectrometry

The ESI-MS spectrum of **CrW_{12}** in negative ion mode in mixed $H_2O/CH_3CN/MeOH$ solution reveals, besides small decomposition species, only the doubly- and triply-charged monolacunary Keggin fragments $H_{7-x-y}Na_xTMA_y[CrW_{11}O_{39}]^{2-}$ (x = 1; y = 1-4) and triple-charged $H_{6-x-y}Na_xTMA_y[CrW_{11}O_{39}]^{3-}$ (x = 1, 2; y = 1, see Fig. S2, Table S2).

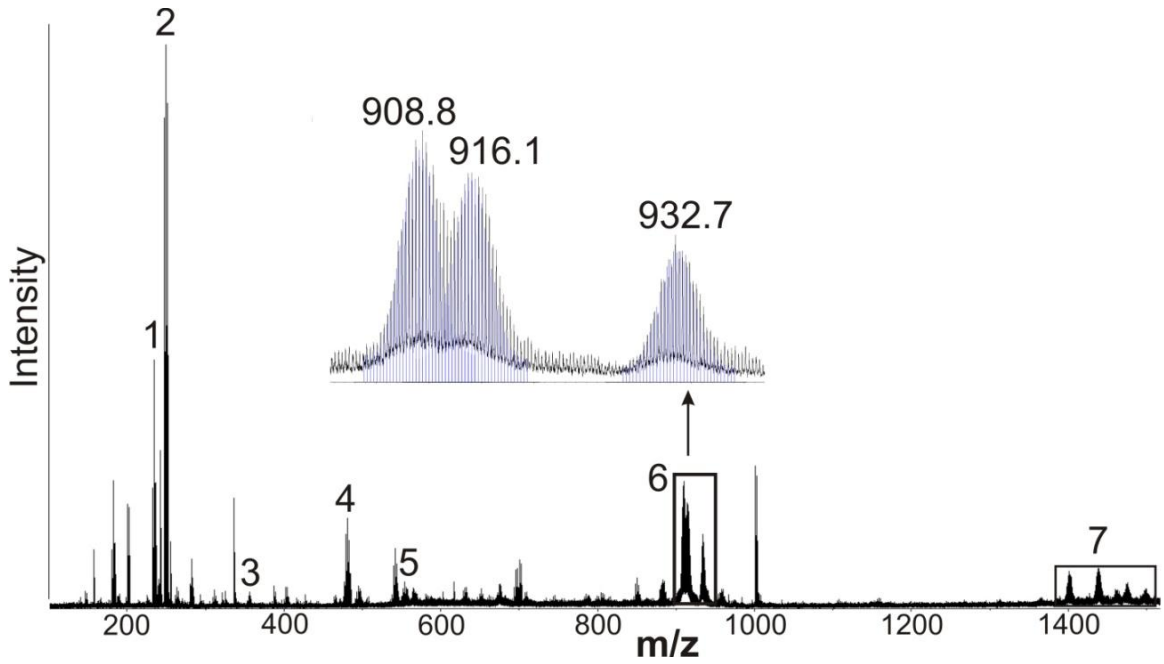

Fig. S2. Negative ion-mode ESI-MS spectrum of **CrW_{12}** in $H_2O/CH_3CN/MeOH$ mixture. ESI-MS peak envelopes of $H_{6-x-y}Na_xTMA_y[CrW_{11}O_{39}]^{3-}$ (TMA – tetramethylammonium, x = 1, 2; y = 1 experimental pattern, black; simulated pattern, blue). See Table S2 for the peaks assignment.

Table S2. Species assigned to the peaks in the ESI-MS spectrum of **CrW_{12}** (see Fig. S2).

	m/z	***m/z* (calc.)**	**peak assignment**
1	239.9	239.9	$[W_2O_7]^{2-}$
2	248.9	248.9	$H[WO_4]^-$
3	355.8	355.8	$[W_3O_{10}]^{2-}$
4	480.9	480.9	$H[W_2O_7]^-$
5	553.9	553.9	$TMA[W_2O_7]^-$
6	908.8	908.8	$H_5Na[CrW_{11}O_{39}]^{3-}$
	916.1	916.1	$H_4Na_2[CrW_{11}O_{39}]^{3-}$
	932.7	932.7	$H_4Na(TMA)[CrW_{11}O_{39}]^{3-}$
7	1400.7	1400.7	$H_5Na(TMA)[CrW_{11}O_{39}]^{2-}$
	1437.2	1437.3	$H_4Na(TMA)_2[CrW_{11}O_{39}]^{2-}$
	1462.9	1462.9	$H_4(TMA)_3[CrW_{11}O_{39}]^{2-}$
	1473.7	1473.3	$H_3Na(TMA)_3[CrW_{11}O_{39}]^{2-}$
	1499.3	1498.9	$H_3(TMA)_4[CrW_{11}O_{39}]^{2-}$

Electrochemistry

The electrochemical behavior of **CrW_{12}** and ammonium metatungstate $(NH_4)_6$**H_2W_{12}** at pH = 7.5 (1 M Na_2SO_4) is shown in Figure S3. The reversible reduction processes observed for both compounds are attributed to the reduction of W^{VI} to W^V. The cyclic voltammogram of **CrW_{12}** exhibits three successive quasi-reversible reduction waves with the half redox potential values $E_{1/2}$ of -0.213, -0.364 and -0.647 V, where $E_{1/2}$ = (Epa + Epc)/2 (Epa and Epc being the anodic and the cathodic peak potentials, respectively). In the cyclic voltammogram of **H_2W_{12}** two reversible waves are present with $E_{1/2}$ = -0.006 V and -0.206 V. The obtained electrochemical data confirmed a known postulate that an increase in the negative charge of the heteropolyanions leads to an increase of the first reduction potential.[13] Thus, more negative potential for **CrW_{12}** (-0.213 V) compared to **H_2W_{12}** (-0.006 V) indicates predomination of Cr-centered anions with charge 5- over (H_2)-centered anion with charge 6- in **CrW_{12}**.

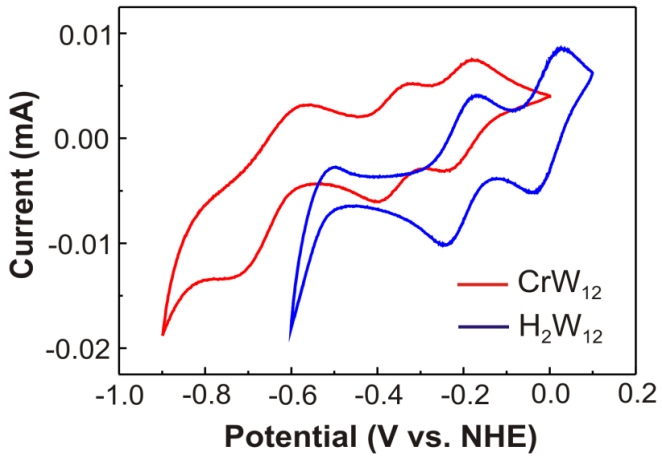

Fig. S3. Cyclic voltammograms of **CrW_{12}** (red line) and $(NH_4)_6$**H_2W_{12}** (blue line) in 1 M Na_2SO_4 at pH 7.5. Working electrode, glassy carbon (d = 3 mm); reference electrode, normal hydrogen electrode (NHE); scan rate, 50 mV s^{-1}; concentration of **CrW_{12}** and **H_2W_{12}**, 2 mM. The scanning is done in the direction of negative potentials.

Thermogravimetric analysis

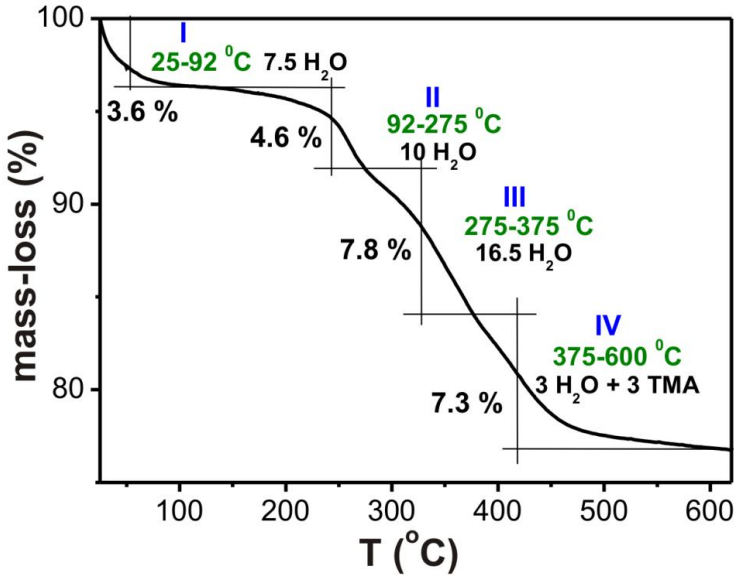

Fig. S4. Thermogravimetric curve of **CrW_{12}** in the temperature region 25 – 610 ºC with a heating rate of 5 ºC min^{-1}.

Powder X-ray diffraction

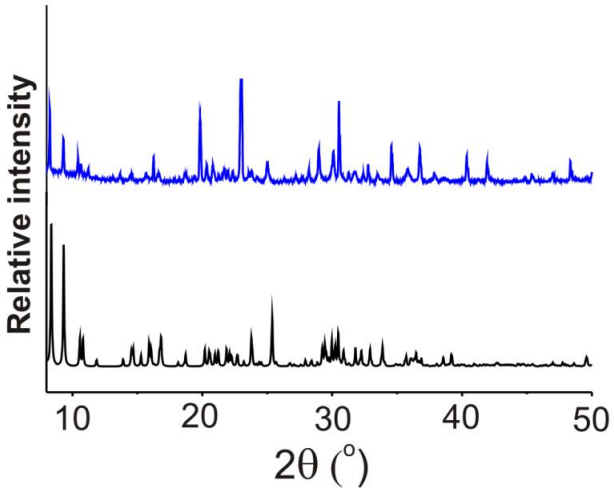

Fig. S5. Experimental (blue) and simulated (black) X-ray diffraction patterns of **CrW_{12}**.

Theoretical studies

Based on the density functional theory (DFT), calculations were performed on the possible arrangements of Cr^{III} in **CrW_{12}**. The calculations revealed that the tetrahedral coordination is more stable by 138.6 kcal/mol than the square-planar.

Usually, complete active space (CAS) calculations allow for estimation of the axial (*D*) and rhombic (*E*/*D*) components of the zfs tensor, as well as the contributions of each excited state to these parameters. Besides the problems in the convergence inherent to this methodology, the study of a large system with a non-evident electronic structure as in **CrW_{12}** complicates the choice of the

adequate and size-limited active space to build the ground and excited states. Despite the inherent difficulties that go with the *ab initio* methods based on CAS approach (the choice of the adequate active space, the limited size of the active space and the slow or deficient convergence), our calculations on **CrW_{12}** with tetrahedral Cr^{III} ion (chemical occupancy 1) worked out reliably. The values found for D (+1.90 cm^{-1}) and E/D ratio (0.180) agreed with the experimental estimations. In a similar way as in tetrahedral d^7 complexes, for an ideal tetrahedral d^3 complexes, with $^4T_1$ ground term, a counterbalance of contributions from a 2nd order spin-orbit coupling leads to a null D value. However, distortions should change this situation. In **CrW_{12}**, the slight loss of symmetry in the $[CrO_4]^{5-}$ unit causes the weak splitting of this term in three quartet states, with one of them being the ground state. Hence, two low-lying excited quartet states interacting significantly with the ground state do not completely cancel their contributions to the zfs tensor. On the other hand, a d^3 configuration in a T_d symmetry displays two excited largely stabilized doublet states coming from a 2E term, that is the energy gap between them and the ground state should be small or moderate at most. However, this is not the case for **CrW_{12}**. A partial charge transfer from the oxo groups to the Cr^{III} ion defines the ground state. This fact is not surprising because two groups largely different in the electronic nature, one with a significant electron excess (oxo ligands) and another one with only partially filled orbitals, particularly in an unstable tetrahedral geometry (metal cation), are connected. This large splitting of the $^4T_1$ ground term weakens the individual contributions to D, being the no cancellation of contributions less perceptible (see Table S4). The good agreement of sign and magnitude of D and E/D ratio with the experimental results is also supported by the values of the components of the g tensor for the $M_S = \pm 1/2$ ground Kramers doublet close to those found by EPR, confirming the positive sign of D ($g_1 = 1.80$, $g_2 = 2.83$ and $g_3 = 4.86$).

AC measurements

The Cole-Cole plots for **CrW_{12}** in the temperature range 2.0-3.0 K under applied dc fields of 1000 (Fig. S9a) and 2500 G (Fig. S9b) exhibit semicircle shapes that can be fitted by using the generalized Debye model. In this model, the α parameter is related to the width of the distribution of the relaxation times and takes values between 1 (denoting an infinitely wide distribution of relaxation times) and 0 (describing a single relaxation process). The resulting values for α cover the ranges 0.092-0.128 for the explored temperatures (Table S3). These values are compatible with relaxation processes with well-defined energy barriers.

EPR measurements

Figure S6 shows a typical X-band spectrum and its simulation. The simulation allowed us to disentangle the D and E zfs parameters, which is seldom possible through magnetometry, and was not possible from HFEPR in our case.

Figure S7 shows a combined set of conventional (X- and Q-band) EPR and HFEPR data points as a 2-dimensional field vs. frequency (or energy) map. This map is simulated using the spin Hamiltonian parameters given in the main text. Only a few turning points were identifiable in HFEPR spectra but those were attributed with confidence to one of the (nominally) forbidden transition in the $S = 3/2$ spin manifold.

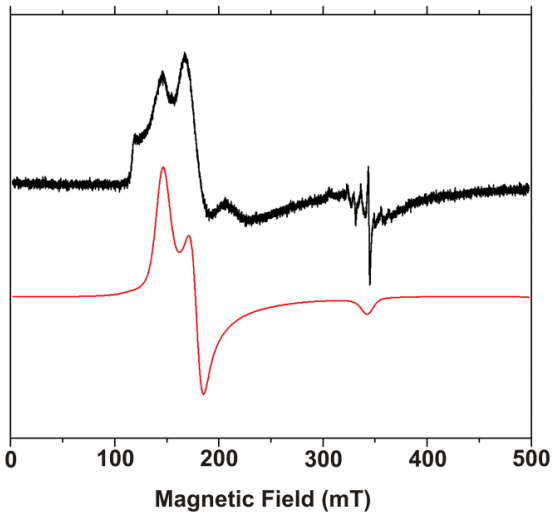

Fig S6. An X-band EPR spectrum of **CrW_{12}** at 9.4 GHz and 10 K (black trace) accompanied by a simulation (red trace) using zfs parameters as in the main text, and g = [2.12, 2.12, 1.97]. Certain features, notably the edge at ca. 118 mT and the line near 200 mT, are not represented in the simulation, which points at a presence of additional spin species, also observed by HFEPR (Fig. 3 in the main text). The sharp resonances near g ~2.0 are radicals and/or defects that are of no concern.

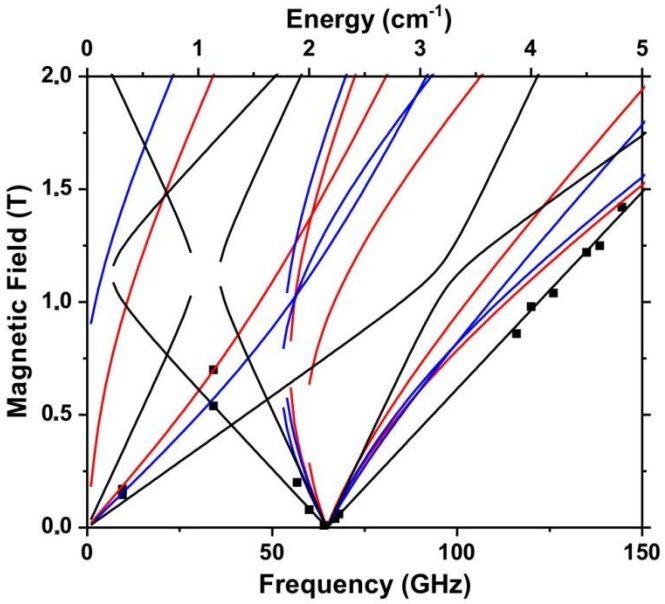

Fig. S7. A field vs. frequency (or energy) dependence of the turning points in the powder spectra of **CrW_{12}** at low temperatures (4.5 – 10 K). The squares are experimental points; the curves are simulations of all possible turning points that can occur in an S = 3/2 spin system using spin Hamiltonian parameters as in the main text. Only the low-field edge of absorption was observable in HFEPR due to poor S/N ratio; however, the simulations confirm the accuracy of the parameters and show that the resonances observed above the zero-field point (65 GHz) are the parallel (B_0 || z-axis of the zfs tensor) turning points of the nominally forbidden $\Delta = \pm 2$ transition such as $|-1/2\rangle \rightarrow |+3/2\rangle$ or $|+1/2\rangle \rightarrow |-3/2\rangle$.

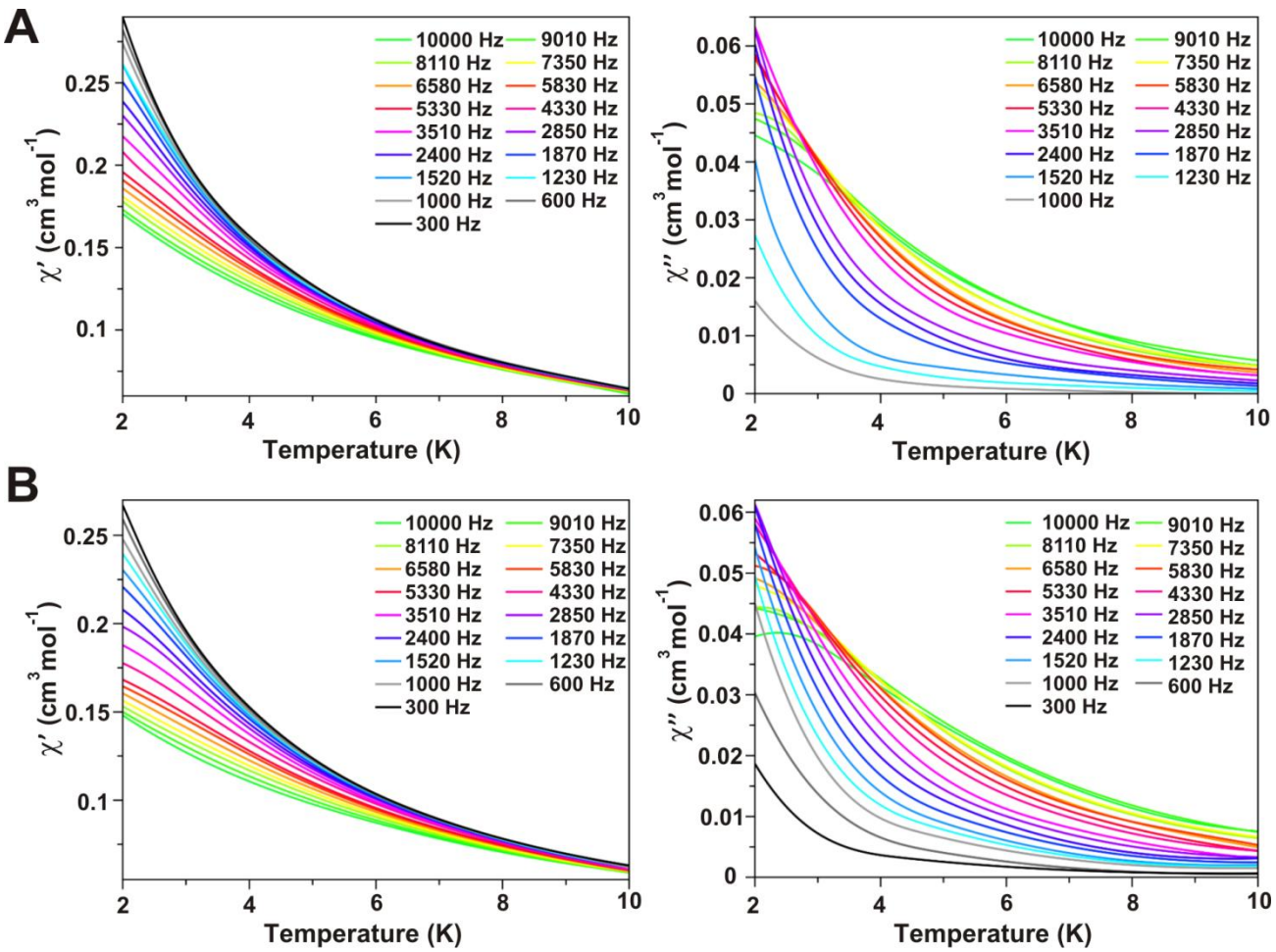

Fig. S8. Temperature dependence of χ'_M (left) and χ''_M (right) of **CrW_{12}** in dc applied field of (A) 1.0 and (B) 2.5 kG and under ± 5.0 G oscillating field at frequencies in the range of 0.6 (black line) to 10.0 (green line) kHz.

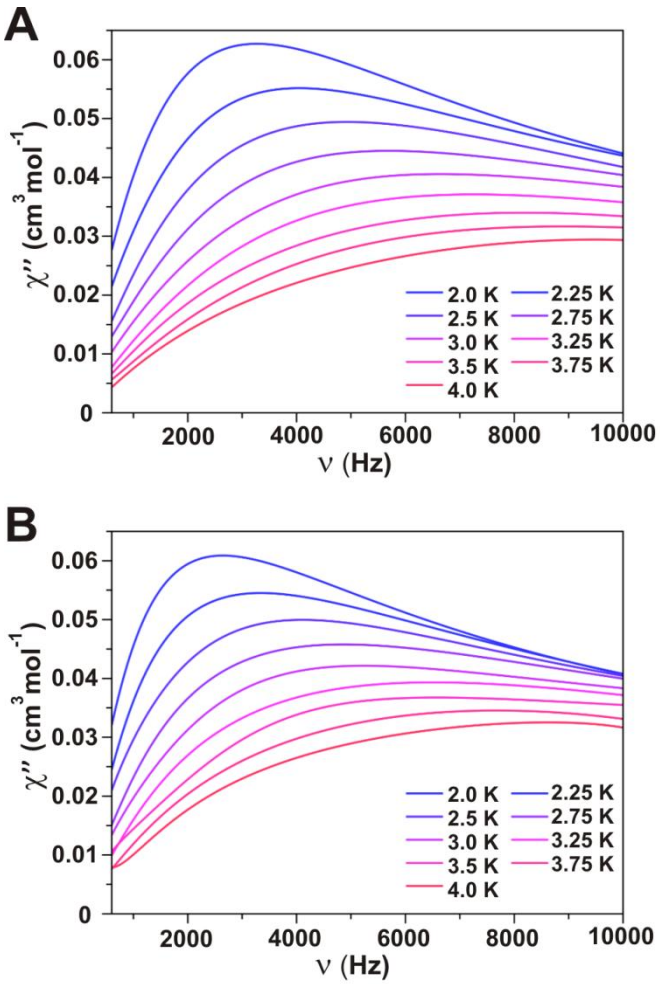

Fig. S9. Dependence of χ''_M of **CrW_{12}** on the frequency (0.3-10.0 kHz) of the oscillating (±5.0 G) dc applied field of (A) 1.0 and (B) 2.5 kG.

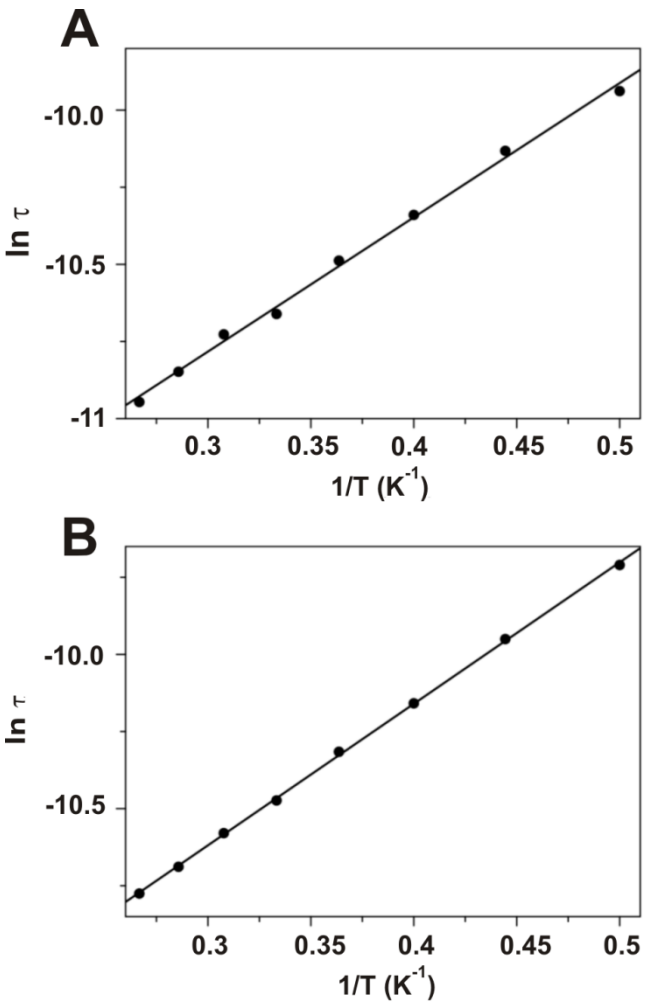

Fig. S10. Arrhenius plots for **CrW_{12}** under an applied static field H_{dc} = 1000 G (A), H_{dc} = 2500 G (B) and with a ±5.0 G oscillating field at frequencies in the range 1.0-10 kHz and the best fit (black line) to a relaxation process governed by an Orbach mechanism (see text).

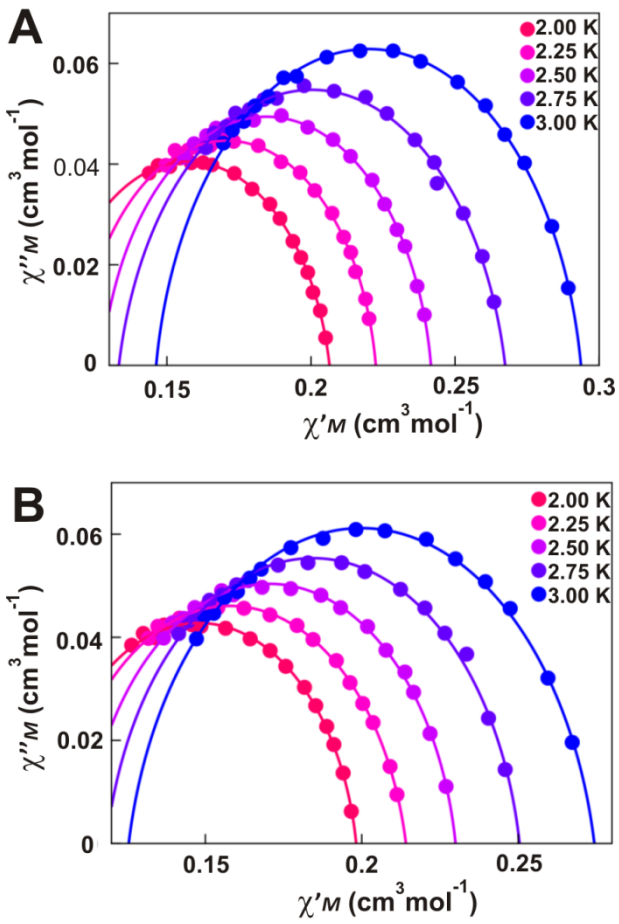

Fig. S11. Cole-Cole plots for **CrW_{12}** in the range from 2.0 to 3.0 K under an applied static field H_{dc} = 1000 G (A) and H_{dc} = 2500 G (B). The solid lines correspond to the best fit according to the Debye model (see Table S3).

XANES analysis

The XANES region at the Cr K-edge, was investigated for **CrW_{12}** and the Anderson type $Na_6[Cr^{III}(OH)_3W_6O_{21}]$[1] as an example of a POT with Cr^{III} in octahedral coordination (Fig. S12). The edge shift for both compounds is calculated at the maximum of the first derivative of the edge and shows the same value of 6001 eV in agreement with literature data for Cr^{III}.[14] The pre-edge peak for 3d-metals, which occurs due to the 1s transition to the p component in d-p hybridized orbital in T_d symmetry or 1s–3d electric quadrupole transition in O_h symmetry, is usually more intense for tetrahedral species than those for octahedral ones.[15] However, the pre-edge peak intensity for a compound with a tetrahedral center changes as a function of the number of 3d electrons. It is maximized at d^0 and gradually decreases to zero at d^{10}. A simple comparison of the pre-edge peak intensities is not appropriate to evaluate the coordination number of Cr^{III} in this case. The distortion of symmetry from O_h in $Na_6[Cr^{III}(OH)_3W_6O_{21}]$ can dramatically enhance the pre-edge peak intensity,[15] and the state of $3d^3$ for Cr^{III} weakens the pre-edge peak intensity compared to T_d symmetry for Cr^{VI}.

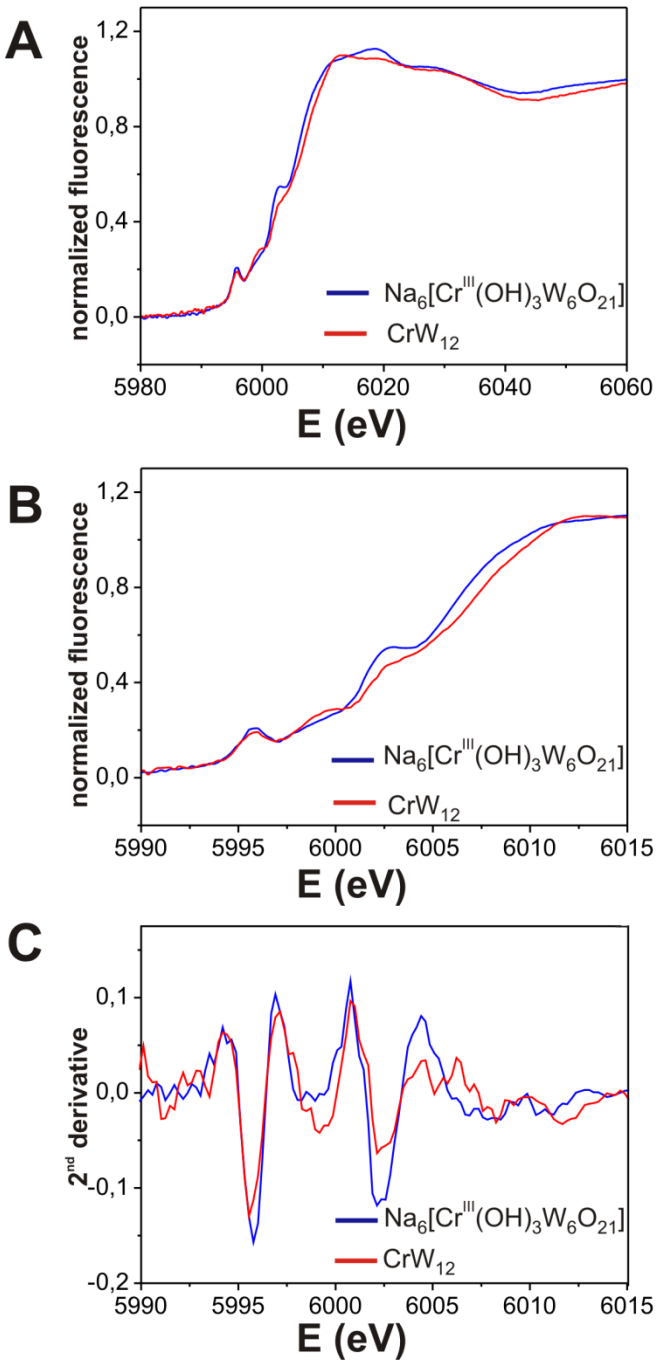

Fig. S12. A) and B) Normalized XANES spectra taken at the Cr K-edge of $Na_6[Cr(OH)_3W_6O_{21}]$ and **CrW_{12}**. C) Second derivatives of the normalized spectra taken at the Cr K-edge of $Na_6[Cr(OH)_3W_6O_{21}]$ and **CrW_{12}**.

X-ray photoelectron spectroscopy (XPS)

To establish the oxidation state of the chromium ion in **CrW_{12}**, XPS spectra were recorded and analyzed. The Cr2p XPS spectrum displays the characteristic peaks $Cr2p_{3/2}$ and $Cr2p_{1/2}$ at 577.3 and 586.9 eV, respectively (Fig. S13) According to a preliminary XPS study on a surface of chromium oxides Cr_2O_3, which evolves during several chemical processes, the binding energy corresponding to the $Cr2p_{3/2}$ line for different oxidation states of chromium sites should be in the ranges 580.7-581.9 (Cr^{VI}), 577.0-577.6 (Cr^{III}), 576.0-576.7 and 574.3 eV (Cr^0).[16] Therefore, it is possible to conclude that the chromium ions in **CrW_{12}** are in plus 3 state.

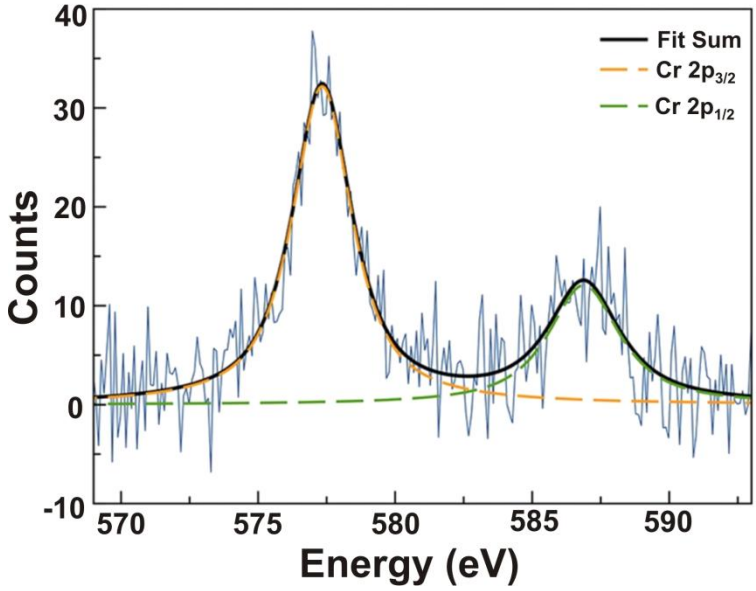

Fig. S13. Cr2p XPS spectrum of **CrW_{12}** taken at the binding energies range (569-593 eV).

UV-vis-NIR electronic spectroscopy

The level diagram for the electronic terms for d^3 or d^7 ions show ^4F and ^4P terms as ground and first excited states. The electronic effect of an electric field induced by ligands coordinated to the metal ion produces a splitting of each of these terms. The resulting Tanabe-Sugano diagrams for d^3 and d^7 ions in tetrahedral and octahedral ligand fields, respectively, are equivalent, being the latter, observed in high-spin cobalt(II) complexes, the most common case in coordination chemistry. The main difference between both cases is the weaker splitting of the d orbitals into e_g and t_{2g} orbitals, provided by the parameter 10*Dq*, in the former case, about 4/9 of the last case. In such ones, the splitting of the ^4F and ^4P terms leads to $^4T_1(F)$, $^4T_2(F)$, $^4A_2(F)$, and $^4T_1(P)$ lower states, which are the ground states for weak or moderate ligand field. The spin-allowed electronic transitions between these states could provide information about the magnitude of the crystal field splitting (10*Dq*) and inter-electronic repulsion parameter (*B*) defined by the crystal field theory. The UV-vis-NIR solid reflectance spectrum of **CrW_{12}** in the range from 350 to 1250 nm (Fig. S14) shows three electronic transitions that were assigned as follows: $^4T_1(F) \rightarrow {}^4T_2(F)$ at 8591 cm^{-1} (ν_1, 1164 nm), $^4T_1(F) \rightarrow {}^4A_2(F)$ at 15528 cm^{-1} (ν_2, 644 nm), and $^4T_1(F) \rightarrow {}^4T_1(P)$ at 23095 cm^{-1} (ν_3, 433 nm). For **CrW_{12}** the values of *Dq* and *B* were obtained from the equations $Dq = (\nu_2 - \nu_1)/10$ and $B = (\nu_3 + \nu_2 - 3\nu_1)/15$ are *Dq* = 693.7 cm^{-1} and *B* = 856.6 cm^{-1}.[17] The low value of *Dq*, about half of those found in high-spin octahedral d^7 complexes, agrees with a tetrahedral ligand field.[18-22] Moreover, the *B* value is substantially lower than that expected for Cr^{III} ion (B_0 = 1030 cm^{-1}), which denotes a significant covalence. This conclusion together with the higher *B* value than the one proposed for a free Cr^{II} ion (830 cm^{-1}) supports a moderate charge-transfer from the oxo groups to

the Cr^{III} ion. The good agreement of these results with the crystal field theory allows us to establish once again the presence of a high-spin d^3 Cr^{III} ion in a tetrahedral coordination environment.

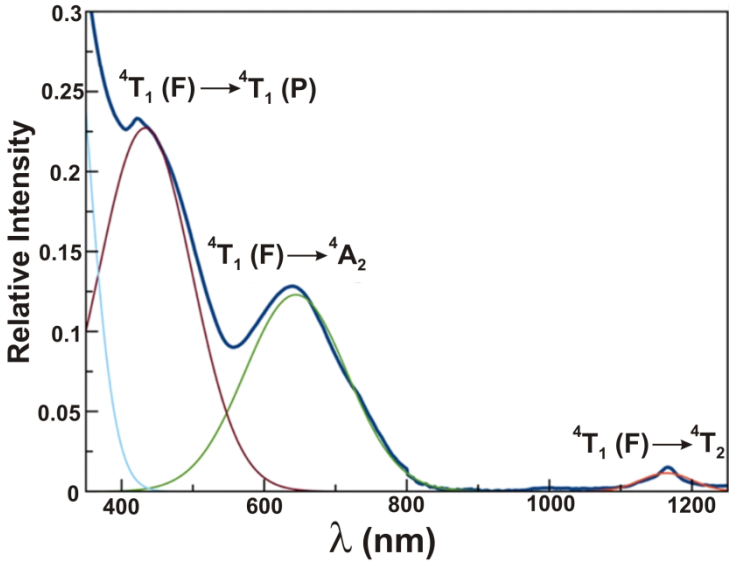

Fig. S14. UV-vis-NIR solid reflectance spectrum of **CrW_{12}**. Thick and thin lines correspond to the experimental and the deconvoluted curves, respectively.

Given that, in an ideal tetrahedral geometry $^4T_1$ is the ground state, the magnetic behavior of **CrW_{12}** could be usually induced by a first order spin-orbit coupling (SOC) by coupling between the orbit (L = 1) and spin (S = 3/2) momenta leading to a splitting into six Kramers doublets in a distorted geometry. The rho parameter is 0.362. In such a case, an approach based on the T-P isomorphism allows to analyze their magnetic properties through the Hamiltonian

$$\boldsymbol{H} = -\alpha\lambda \boldsymbol{L}_{Co}\boldsymbol{S}_{Co} + \Delta\left[\boldsymbol{L}_{z,Co}^2 - \frac{1}{3}L(L+1)\right] + \beta H(-\alpha \boldsymbol{L}_{Co} + g_e \boldsymbol{S}_{Co}) \qquad (\mathbf{1}),^{23}$$

where λ and α are the spin-orbit coupling constant and the orbital reduction factor defined as $\alpha = A\kappa$. Parameters κ and A account for the reduction of the orbital momentum caused by the delocalization of the unpaired electrons, and the admixture between the $^4T_1$(P) excited and $^4T_1$(F) ground states (A takes values of 1.5 and 1 in the weak and strong crystal-field limits, respectively). Finally, distortion in the tetrahedral coordination sphere leads to a splitting of the $^4T_1$(F) ground state into orbital singlet ($^4A_2$) and doublet (^4E) levels, being quantified by the Δ parameter. Best-fit parameters of the thermal dependence on $\chi_M T$ of **CrW_{12}** below 30 K are: α = 1.09, λ = +66.5 cm^{-1}, Δ = +3175 cm^{-1}, TIP = –2326 x 10^{-6} cm^3 mol^{-1} with F = 5.4 x 10^{-5} (TIP is the temperature-independent paramagnetism and F is the agreement factor defined as $\sum[P_{exp}-P_{calcd}]^2/\sum[P_{exp}]^2$ where P is the physical property under study). The low values of λ and α are remarkable, being the former largely lower than the value for the free ion (λ_0 = –91 cm^{-1}) From the values of Dq and B determined for **CrW_{12}** taken from the analysis of their UV-vis-NIR spectra (see above), a value of A equal to 1.44 for **1** and **2** can be calculated through equation[23]:

$$c = 0.75 + 1.875(B/Dq) - 1.25\sqrt{1 + 1.8(B/Dq) + 2.25(B/Dq)^2}$$
$$A = (1.5 - c^2)/(1 + c^2)$$

From the values of α and A previously obtained, κ is found to be equal to 0.76. The values of κ (0.76) and λ/λ_0 (0.74) and B/B_0 (0.83) ratios agree with the strong covalence previously postulated for **CrW_{12}**.

Table S3. Selected ac magnetic data for **CrW_{12}** at different dc applied fields.

Compound	H^a (G)	$\tau_0{}^b \times 10^6$ (s)	$E_a{}^b$ (cm^{-1})	α^c	$\chi_S{}^c$ (cm^3 mol^{-1})	$\chi_T{}^c$ (cm^3 mol^{-1})
CrW_{12}	1000	5.62(21)	3.03(7)	0.122(7) [3.00 K] 0.094(9) [2.75 K] 0.092(5) [2.50 K] 0.128(2) [2.25 K] 0.101(5) [2.00 K]	0.108(2) [3.00 K] 0.119(2) [2.75 K] 0.127(2) [2.50 K] 0.133(2) [2.25 K] 0.146(2) [2.00 K]	0.2064(2) [3.00 K] 0.2225(2) [2.75 K] 0.2416(2) [2.20 K] 0.2674(5) [2.25 K] 0.2937(3) [2.00 K]
CrW_{12}	2500	6.17(8)	3.19(24)	0.104(8) [3.00 K] 0.126(6) [2.75 K] 0.105(8) [2.50 K] 0.112(2) [2.25 K] 0.124(9) [2.00 K]	0.098(2) [3.00 K] 0.102(2) [2.75 K] 0.111(2) [2.50 K] 0.118(2) [2.25 K] 0.126(2) [2.00 K]	0.1988(3) [3.00 K] 0.2141(3) [2.75 K] 0.2300(3) [2.20 K] 0.2504(6) [2.25 K] 0.2743(6) [2.00 K]

[a] Applied dc magnetic field. [b] The values of the pre-exponential factor (τ_0) and activation energy (E_a) are calculated through the Arrhenius law [$\tau^{-1} = \tau_0{}^{-1} \exp(-E_a/k_BT)$]. [c] The values of the α parameter, adiabatic (χ_S) and isothermal (χ_T) susceptibilities are calculated from the experimental data at different temperatures through the generalized Debye law (see text).

Table S4. Energy of the calculated quartet (Q_i) and triplet (D_i) excited states and their contributions to the *D* and *E* values for **CrW_{12}** obtained from CASSCF/NEVPT2 calculations. D_{SS} is the spin-spin contribution to axial zfs parameter, and D_Q and D_D are the sum of spin-orbit contributions coming from quartet and doublet excited states.

State	Energy[a]	*S*	*D*[a]	*E*[a]	State	Energy[a]	*S*	*D*[a]	*E*[a]
D_{SS}		4	0.000	0.000	D_5	16669.0	2	0.014	-0.000
D_Q		4	0.677	-0.059	D_6	18656.5	2	-0.144	-0.012
D_D		2	1.176	0.387	D_7	20370.4	2	-0.014	0.015
Q_1	4877.8	4	1.030	-0.127	D_8	21212.1	2	0.137	0.001
Q_2	9491.2	4	-0.646	0.000	D_9	23879.9	2	0.024	-0.024
Q_3	17307.2	4	0.446	0.232	D_{10}	24273.3	2	0.010	-0.032
Q_4	19729.5	4	-0.254	-0.008	D_{11}	25763.1	2	0.057	0.000
Q_5	20501.4	4	0.131	-0.148	D_{12}	28851.7	2	-0.136	-0.058
Q_6	27894.9	4	-0.013	0.000	D_{13}	29330.4	2	-0.116	-0.121
Q_7	29270.4	4	-0.027	0.000	D_{14}	30256.2	2	0.383	-0.003
Q_8	31883.4	4	0.011	-0.008	D_{15}	30679.9	2	-0.154	0.150
Q_9	37796.9	4	-0.001	0.000	D_{16}	32806.5	2	0.104	-0.001
D_1	5955.2	2	1.732	-0.000	D_{17}	34110.3	2	0.040	0.001
D_2	6626.9	2	-0.679	0.422	D_{18}	34485.6	2	-0.060	0.055
D_3	14516.7	2	0.002	-0.000	D_{19}	35816.2	2	0.000	-0.000
D_4	16268.8	2	-0.064	-0.003	D_{20}	37004.2	2	0.040	-0.003

[a]Values in cm^{-1}.

Table S5. Selected magnetic characteristics for POM-based and 3d transition metals based SIMs/SMMs.

Compound	SIM, $H = 0$	SIM, $H \neq 0$	*U*eff/K	τ_0/s	Ref.
$Cr^{III}W_{12}$	No	1000 G	3	5.6×10^{-6}	this work
Cr^{II}-based SIMs					
$[Cr^{II}(N(TMS)_2)_2(py)_2]$	No	1500 G	9	1.4×10^{-5}	24
$[Cr^{II}(N(TMS)_2)_2(THF)_2]$	No	2500 G	11.8	2.7×10^{-6}	24
d-block SIMs based on POMs					
$TBA_7H_{10}[Fe^{III}(A\text{-}\alpha\text{-}SiW_9O_{34})_2]$	No	1000 G	9.2	3.3×10^{-6}	25
$TBA_7H_{11}[Co^{II}(A\text{-}\alpha\text{-}SiW_9O_{34})_2]$	No	1000 G	19.3	8.2×10^{-6}	25
f-block SIMs based on POMs					
$Na_9[ErW_{10}O_{36}]$	No	1000 G	55.2	1.6×10^{-8}	26
$[TBA]_5[Dy(Mo_8O_{26})_2]$	No	1000 G	38.5	6.6×10^{-8}	27
$[TBA]_5[Yb(Mo_8O_{26})_2]$	No	1000 G	23.3	6.7×10^{-6}	27
SMMs based on POMs					
$Na_4K(C_4H_{10}NO)_7\{[GeW_9O_{34}]_2[Mn^{III}{}_4Mn^{II}{}_2O_4(H_2O)_4]\}$	No	1000 G	14.8	3.1×10^{-7}	28
$Na_6(C_4H_{12}N)_4[Fe^{III}{}_{14}(H_2O)_2(Fe^{III}W_9O_{34})_2]$	No	1000 G	16.7	2×10^{-6}	29
$Na_{22}Rb_6[\{Co^{II}{}_4(OH)_3PO_4\}_4(A\text{-}\alpha\text{-}PW_9O_{34})_4]$	No	1000 G	26.1	3.5×10^{-8}	30

*SIM, $H = 0$ – SIM behavior in the absence of a dc field;
SIM, $H \neq 0$ – SIM behavior under an applied dc field;
Ueff – effective thermal energy barrier;
τ_0 – pre-exponential factor;
TMS = $SiMe_3$, py = pyridine, THF = tetrahydrofuran, TBA = tetrabutylammonium.

References

1. N. I. Gumerova, T. Caldera Fraile, A. Roller, G. Giester, M. Pascual-Borràs, C. A. Ohlin, A. Rompel, Direct single- and double-side triol-functionalization of the mixed type Anderson polyoxotungstate $[Cr(OH)_3W_6O_{21}]^{6-}$. *Inorg. Chem.* **2019**, *58*, 106-113; doi: 10.1021/acs.inorgchem.8b01740
2. M. J. Frisch, G. W. Trucks, H. B. Schlegel, G. E. Scuseria, M. A. Robb, J. R. Cheeseman, G. Scalmani, V. Barone, B. Mennucci, G. A. Petersson, H. Nakatsuji, M. Caricato, X. Li, H. P. Hratchian, A. F. Izmaylov, J. Bloino, G. Zheng, J. L. Sonnenberg, M. Hada, M. Ehara, K. Toyota, R. Fukuda, J. Hasegawa, M. Ishida, T. Nakajima, Y. Honda, O. Kitao, H. Nakai, T. Vreven, J. A. Montgomery, Jr., J. E. Peralta, F. Ogliaro, M. Bearpark, J. J. Heyd, E. Brothers, K. N. Kudin, V. N. Staroverov, R. Kobayashi, J. Normand, K. Raghavachari, A. Rendell, J. C. Burant, S. S. Iyengar, J. Tomasi, M. Cossi, N. Rega, J. M. Millam, M. Klene, J. E. Knox, J. B. Cross, V. Bakken, C. Adamo, J. Jaramillo, R. Gomperts, R. E. Stratmann, O. Yazyev, A. J. Austin, R. Cammi, C. Pomelli, J. W. Ochterski, R. L. Martin, K. Morokuma, V. G. Zakrzewski, G. A. Voth, P. Salvador, J. J. Dannenberg, S. Dapprich, A. D. Daniels, Ö. Farkas, J. B. Foresman, J. V. Ortiz, J. Cioslowski, D. J. Fox, Gaussian-09, Gaussian, Inc., Wallingford CT, (2016).
3. J. P. Perdew, K. Burke, M. Ernzerhof, Generalized gradient approximation made simple. *Phys. Rev. Lett.* **1996**, *77*, 3865-3868. doi: 10.1103/PhysRevLett.78.1396
4. A. Schaefer, H. Horn, R. Ahlrichs, Fully optimized contracted Gaussian basis sets for atoms Li to Kr. *J. Chem. Phys.* **1992**, *97*, 2571-2577. doi: 10.1063/1.463096

5. P. J. Hay, W. R. Wadt, *Ab initio* effective core potentials for molecular calculations. Potentials for K to Au including the outermost core orbitals. *J. Chem. Phys.* ***1985****, 82,* 299-310. doi: 10.1063/1.448975
6. J. Tomasi, B. Mennucci, E. Cancès, The IEF version of the PCM solvation method: an overview of a new method addressed to study molecular solutes at the QM ab initio level. *J. Mol. Struct. Theochem.* **1999**, *464*, 211–226. doi: 10.1016/S0166-1280(98)00553-3
7. F. Neese, The ORCA program system. *WIREs Comput. Mol. Sci.* **2012**, *2*, 73-78. doi: 10.1002/wcms.81
8. K. Eichkorn, O. Treutler, H. Ohm, M. Haser, R. Ahlrichs, Auxiliary basis sets to approximate Coulomb potentials. *Chem. Phys. Lett*. **1995**, *240*, 283-290. doi: 10.1016/0009-2614(95)00621-A
9. S. Vancoillie, J. Chalupský, U. Ryde, E. I. Solomon, K. Pierloot, F. Neese, L. Rulíšek, Multireference *Ab Initio* calculations of g tensors for trinuclear copper clusters in multicopper oxidases. *J. Phys. Chem. B* **2010**, *114*, 7692-7702. doi: 10.1021/jp103098r
10. S. Kossmann, F. Neese, Efficient structure optimization with second-order many-body perturbation theory: The RIJCOSX-MP2 method. *J. Chem. Theory Comput*. **2010**, *6*, 2325-2338. doi: 10.1021/ct100199k
11. S. Kossmann, F. Neese, Comparison of two efficient approximate Hartee–Fock approaches. *Chem. Phys. Lett*. **2009**, *481*, 240-243. doi: 10.1016/j.cplett.2009.09.073
12. A. K. Hassan, L. A. Pardi, J. Krzystek, A. Sienkiewicz, P. Goy, M. Rohrer, L.-C. Brunel, Ultrawide band multifrequency high-field EMR technique: a methodology for increasing spectroscopic information. *J. Magn. Reson.* **2000,** *142*, 300-312. doi: 10.1006/jmre.1999.1952
13. M. Sadakane, E. Steckhan, Electrochemical properties of polyoxometalates as electrocatalysts. *Chem. Rev.* **1998**, *98*, 219-238. doi: 10.1021/cr960403a
14. M. Tromp, J. Moulin, G. Reid, J. Evans, Cr K-Edge XANES spectroscopy: ligand and oxidation state dependence – what is oxidation state? *AIP Conference Proceedings* **2007**, *882*, 699-702. doi: 10.1063/1.2644637
15. T. Yamamoto. Assignment of pre-edge peaks in K-edge x-ray absorption spectra of 3d transition metal compounds: electric dipole or quadrupole? *X-Ray Spectrom.* **2008**, *37*, 572-584. doi: 10.1002/xrs.1103
16. B. P. Liu, P. Sindelar, Y. W. Fang, K. Hasebe, M. Terano, Correlation of oxidation states of surface chromium species with ethylene polymerization activity for Phillips CrO_x/SiO_2 catalysts modified by Al-alkyl cocatalyst. *J. Mol. Catal. A: Chem.* **2005**, *238*, 142-150. doi:10.1016/j.molcata.2005.05.015
17. A. B. P. Lever, *Inorganic Electronic Spectroscopy*, Elsevier, Amsterdam, 1984.
18. A. A Razik, A. K. Abdel Hadi, Synthesis and spectral studies of chromium(III), cobalt(II) and nickel(II) complexes with phenylhydrazonoamidoxime *Transition Metal Chem.* **1994**, *19*, 84-86. doi: 10.1007/BF00166275
19. M. A. Maldonado-Rogado, E. Viñuelas-Zahínos, F. Luna-Giles, F. J. Barros-García, Synthesis and structural characterization of cobalt(II) and zinc(II) complexes with 2-(indazol-1-yl)-2-thiazoline (TnInA). X-ray characterization of $[CoCl_2(TnInA)_2]\cdot C_2H_6O$ and $[(M)(TnInA)_2(H_2O)_2](NO_3)_2$ (M = Co, Zn). *Polyhedron* **2007**, *26*, 5210-5218. doi: 10.1016/j.poly.2007.07.043
20. D. Shukla, L. K. Gupta, S. Chandra, Spectroscopic studies on chromium(III), manganese(II), cobalt(II), nickel(II) and copper(II) complexes with hexadentate nitrogen-sulfur donor [N(2)S(4)] macrocyclic ligand. *Spectrochim. Acta A* **2008**, *71*, 746-750. doi: 10.1016/j.saa.2007.12.052

21. E. Soleimani, Synthesis, characterization and anti-microbial activity of a novel macrocyclic ligand derived from the reaction of 2,6-pyridinedicarboxylic acid with homopiperazine and its Co(II), Ni(II), Cu(II), and Zn(II) complexes. *J. Mol. Struct.* **2011**, *995*, 1-8. doi: 10.1016/j.molstruc.2011.01.002
22. A. Świtlicka, J. Palion-Gazda, B. Machura, J. Cano, F. Lloret, M. Julve. Field-induced slow magnetic relaxation in pseudooctahedral cobalt(ii) complexes with positive axial and large rhombic anisotropy. *Dalton Trans.* **2019**, *48*, 1404-1417. doi: 10.1039/C8DT03965H
23. F. Lloret, M. Julve, J. Cano, E. Pardo, Magnetic properties of six-coordinated high-spin cobalt(II) complexes: Theoretical background and its application. *Inorg. Chim. Acta*, **2008**, *361*, 3432-3445. doi: 10.1016/j.ica.2008.03.114
24. Y.-F. Deng, T. Han, Z. Wang, Z. Ouyang, B. Yin, Z. Zheng, J. Krzystek, Y.-Z. Zheng, Uniaxial magnetic anisotropy of square-planar chromium(II) complexes revealed by magnetic and HF-EPR studies. *Chem. Commun.* **2015**, *51*, 17688-17691. doi: 10.1039/c5cc07025b
25. R. Sato, K. Suzuki, T. Minato, M. Shinoe, K. Yamaguchi, N. Mizuno, Field-induced slow magnetic relaxation of octahedrally coordinated mononuclear Fe(III)-, Co(II)-, and Mn(III)-containing polyoxometalates. *Chem. Commun.* **2015**, *51*, 4081-4084. doi: 10.1039/C4CC09435B
26. M. A. AlDamen, J. M. Clemente-Juan, E. Coronado, C. Martí-Castaldo, A. Gaita-Ariño, Mononuclear lanthanide single-molecule magnets based on polyoxometalates. *J. Am. Chem. Soc.* **2008**, *130*, 8874-8875. doi: 10.1021/ja801659m
27. J. J. Baldoví, Y. Duan, C. Bustos, S. Cardona-Serra, P. Gouzerh, R. Villanneau, G. Gontard, J. M. Clemente-Juan, A. Gaita-Ariño, C. Giménez-Saiz, A. Proust, E. Coronado, Single ion magnets based on lanthanoid polyoxomolybdate complexes. *Dalton Trans.* **2016**, *45*, 16653-16660. doi: 10.1039/C6DT02258H
28. C. Ritchie, A. Ferguson, H. Nojiri, H. N. Miras, Y.-F. Song, D.-L. Long, E. Burkholder, M. Murrie, P. Kögerler, E. K. Brechin, L. Cronin, Polyoxometalate-mediated self-assembly of single-molecule magnets: $\{[XW_9O_{34}]_2[Mn(III)_4Mn(II)_2O_4(H_2O)_4]\}^{12-}$. *Angew. Chem.* **2008**, 47, 5609-5612. doi: 10.1002/anie.200801281
29. J.-D. Compain, P. Mialane, A. Dolbecq, I. M. Mbomekallé, J. Marrot, F. Sécheresse, E. Rivire, G. Rogez, W. Wernsdorfer, Iron polyoxometalate single-molecule magnets. *Angew. Chem.* **2009**, *121*, 3123-3127. doi: 10.1002/ange.200900117
30. M. Ibrahim, Y. Lan, B. S. Bassil, Y. Xiang, A. Suchopar, A. K. Powell, U. Kortz, Hexadecacobalt(II)-containing polyoxometalate-based single-molecule magnet. *Angew. Chem., Int. Ed.* **2011**, *50*, 4708-4711. doi: 10.1002/anie.201100280